

# Turbulent dissipation in a near-field river plume: A comparison of control volume and microstructure observations with a numerical model

Daniel G. MacDonald,<sup>1,2</sup> Louis Goodman,<sup>1,2</sup> and Robert D. Hetland<sup>3</sup>

Received 22 December 2006; revised 23 March 2007; accepted 10 May 2007; published 25 July 2007.

[1] Data collected from the near-field region (first several kilometers) of the Merrimack River plume are analyzed to provide estimates of turbulent kinetic energy (TKE) dissipation rates. Measurement techniques included a control volume method incorporating density and velocity survey data, and direct dissipation rate measurements by turbulence sensors mounted on an autonomous underwater vehicle (AUV). These two distinct observational approaches are compared with TKE dissipation rates derived from a highly resolved three-dimensional numerical model. In general, there is good agreement between the three estimates of dissipation rate. Differences occurred in two regions: (1) at the base of the plume, where plume density increased, and (2) in the very near field of the plume, which is characterized by rapid acceleration and strong shoaling. Results suggest that there is a feedback between the turbulence and the plume evolution with the result that the spreading rate of the plume is constrained. A scaling parameterization, relating turbulent dissipation rate to plume density and velocity, is also examined. Immediately seaward of the front this parameterization appears to be consistent with observed rates of dissipation, but progressing seaward, a modification to the parameterization may be necessary to account for plume spreading and deepening.

**Citation:** MacDonald, D. G., L. Goodman, and R. D. Hetland (2007), Turbulent dissipation in a near-field river plume: A comparison of control volume and microstructure observations with a numerical model, *J. Geophys. Res.*, *112*, C07026, doi:10.1029/2006JC004075.

## 1. Introduction

[2] The process of turbulence occurs over a wide range of scales [e.g., *Richardson*, 1920], from the largest energy containing scales,  $L_e$ , where energy from the mean flow is typically imparted to the turbulence, down to the Kolmogorov microscales, where turbulent energy is ultimately dissipated into heat. Additionally, the impact of turbulence can also be observed across scales much larger than the energy containing scales, as the cumulative effect of mixing processes and the dissipation of energy originally derived from the mean flow can result in significant alterations to the density structure and momentum of the flow field. As such, it could be argued that turbulence is truly a phenomenon which is important across all scales of relevance to a particular flow field.

[3] A key theoretical relationship in quantifying turbulence observations has been the usage of the steady state turbulent kinetic energy budget equation [*Gregg*, 1987]. However, up until recently the only technique which has been typically employed in turbulence measurements involved estimating one term of the TKE budget, the dissipation rate  $\varepsilon$ . The standard technique to directly measure  $\varepsilon$  is the thrust probe sensor, originally developed by *Siddon* [1965] and initially employed in the ocean by *Osborn* [1974]. Typically this type of measurement is made by a vertical profiler. Recently a number of alternative techniques and platforms have been developed and used to measure ocean turbulence. (For a review of such techniques, see *Lueck et al.* [2002]). One such platform which is particularly useful for inferring  $\varepsilon$  at very high resolution, both horizontally as well as vertically, is an AUV [*Levine et al.*, 1997]. Recently, *Goodman et al.* [2006] have shown that the thrust probe can be successfully mounted on such a platform and produce very high quality measurements of dissipation rate by employing a procedure which corrects sensor vibration and vehicle motion effects arising from all directions. The approach of using micro- and fine-scale sensors on an AUV is particularly useful for measuring turbulence and its local background processes in a field of limited horizontal and vertical extent, such as in buoyant plumes and coastal fronts.

<sup>1</sup>Department of Estuarine and Ocean Sciences, School for Marine Science and Technology, University of Massachusetts-Dartmouth, New Bedford, Massachusetts, USA.

<sup>2</sup>University of Massachusetts School of Marine Sciences, Lowell, Massachusetts, USA.

<sup>3</sup>Department of Oceanography, Texas A&M University, College Station, Texas, USA.

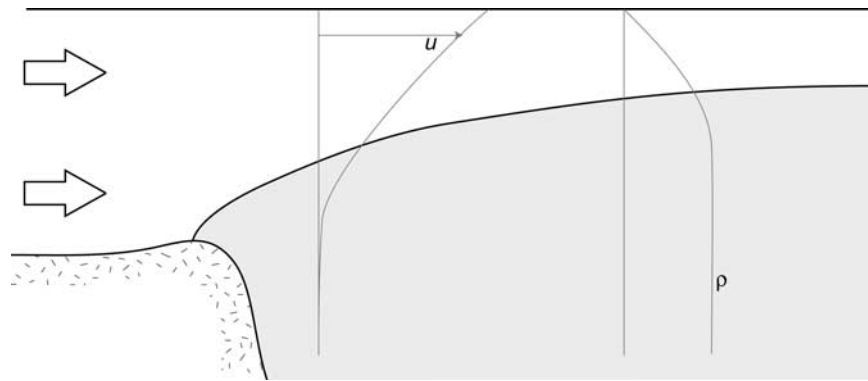


**Figure 1.** Cartoon of vertical structure of near-field plume region, showing velocity and density profiles. Shaded region represents ambient ocean water, while unshaded region represents river and plume water. Vertical mixing between the two water masses, which occurs along the interface, is not represented by the shading.

[4] Recently a technique has been developed [MacDonald and Geyer, 2004; Chen and MacDonald, 2006] to obtain the other terms in the steady state TKE budget equation, namely the buoyancy flux,  $B$ , and shear production,  $P$ , terms. The technique involves using density and velocity transect data collected at scales significantly larger than the energy containing scales [Kay and Jay, 2003; MacDonald and Geyer, 2004; Chen and MacDonald, 2006]. A budget is formed over some finite region of the flow field, or control volume, allowing the turbulent momentum (Reynolds stress) and buoyancy fluxes to be inferred. Owing to the sensitivity required in identifying changes in flow structure, these techniques are best suited for high-energy environments, such as estuaries, and near-field river plumes, where velocities are high and stratification is strong.

[5] Numerical models can also be useful in understanding the vertical and horizontal structure of turbulent fields [e.g., Burchard and Baumert, 1995; Burchard et al., 2002]. Traditional two equation turbulence models [e.g., Galperin et al., 1988; Rodi, 1987], as well as recent advances in turbulence modeling, such as the generic length-scale approach [Umlauf and Burchard, 2003], have proven effective in many cases. However, such second moment closure schemes are based on one-dimensional boundary layer physics, and for energetic shear-stratified flows, the modeled turbulent field will be primarily dependent on the stability functional. Shear-stratified turbulence, particularly in high-energy regimes, remains the major weakness of second moment closure schemes, and it is unclear how accurately these models can predict the magnitude of TKE dissipation rates and other important TKE parameters.

[6] This paper describes measurements of TKE parameters in the highly sheared outflow associated with a near-field river plume [e.g., Wright and Coleman, 1971]. Such a region is characterized by supercritical flow extending several kilometers seaward of a sharp bottom attached salt front, typically located at the mouth of narrow estuaries during high-discharge events (Figure 1). In this environment, high stratification and strong velocity shears create a very active turbulent field, which results in rapid mixing of the discharging water with ambient ocean waters. Previous observations have suggested that mixing is accomplished in this environment primarily through the generation of

Kelvin-Helmholz instabilities [Geyer and Farmer, 1989; MacDonald and Geyer, 2004], resulting in energy containing scales of the turbulence of similar size to the Ozmidov scale ( $L_O = (\varepsilon N^{-3})^{1/2}$ , where  $N$  is the buoyancy frequency).

[7] In this manuscript, estimates of TKE quantities are derived using the control volume technique described by MacDonald and Geyer [2004], and compared with direct estimates of dissipation rates generated from microstructure instrumentation mounted in a horizontal configuration on an AUV, and also with quantities generated from a numerical model of the near-field region. The results provide important insight into the evolution of the turbulent field across the near-field plume region, as well as an opportunity for comparison and validation of two relatively new measurement techniques, and model output. In theory, the fundamental difference in scales associated with the measurement techniques can also be exploited to further understand the heterogeneity of the turbulence field.

[8] A description of the Merrimack River field study and sampling efforts is described in section 2. Section 3 provides a detailed description of the various measurement techniques and the numerical model, and presents results. Comparisons between the observed and modeled turbulent quantities are discussed in section 4, along with implications for the evolution of the near-field plume structure.

## 2. Merrimack River Field Site

[9] Field observations were conducted in the near-field region of the Merrimack River plume on 21 May 2006. The Merrimack River discharges into the Gulf of Maine approximately 6 km south of the New Hampshire–Massachusetts border (see inset, Figure 2), with a watershed covering a significant portion of the New Hampshire and northeast Massachusetts land area. The study occurred less than a week after extensive flooding in the Merrimack River basin resulted in a discharge of nearly  $3000 \text{ m}^3 \text{ s}^{-1}$ , the highest in nearly 70 years. Discharge during the observation period was approximately  $1260 \text{ m}^3 \text{ s}^{-1}$ . Discharges were measured at USGS gauging station number 01100000 in Lowell, Massachusetts, 60 km upstream from the river mouth.

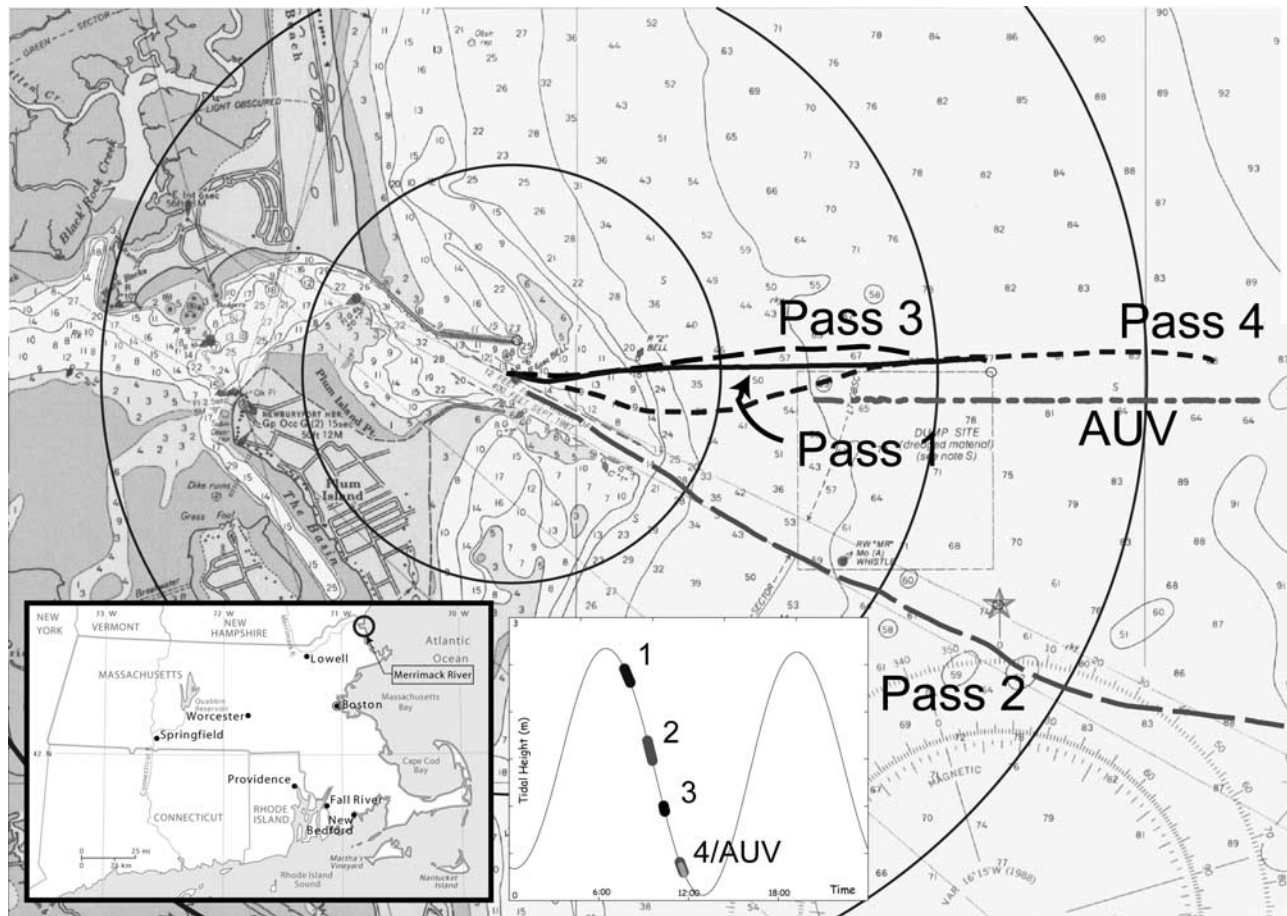


**Figure 2.** Location of sampling passes at mouth of Merrimack River. Passes 1 through 4 indicate locations of CTD/ADCP transects performed from the R/V *Lucky Lady*. The line marked AUV indicates the location of the microstructure AUV run. Concentric circles indicate 1 km radii from the river mouth. Insets show the location of the Merrimack River mouth, near the Massachusetts–New Hampshire border, and the timing of the passes with respect to the tidal cycle on 21 May 2006. The AUV pass occurred at the same time as Pass 4, as shown. Base map is from NOAA chart 13282 (December 1995).

[10] Hydrographic data were collected from the University of Massachusetts research vessel, the R/V *Lucky Lady*, using a towed conductivity temperature depth (CTD) unit (Ocean Sensors, OS200), and two RD Instruments 1200 kHz acoustic Doppler current profilers (ADCPs). One of the ADCPs was mounted in a downward looking position off the starboard side of the research vessel, the other in an upward looking orientation on an Acrobat (Sea Sciences, Inc.) tow body, which was towed approximately 3 m off the starboard side of the vessel at a depth of approximately 4 m. The upward looking ADCP provided critical near surface velocity data which could not be resolved by the downward looking ADCP. The CTD sampled continuously at approximately 6 Hz, providing vertical resolution generally on the order of 5 to 10 cm. The up and down motion of the tow-yo sampling pattern also provided resolution in the horizontal of approximately 100 m. Both ADCP units were sampling at approximately 1 Hz, using 25 cm vertical bins. In addition, a REMUS AUV equipped with microstructure probes (Figure 3) was deployed from a separate vessel.

[11] The location of five sampling transects are shown in Figure 2. Passes 1 through 4 were conducted with the sampling equipment aboard the R/V *Lucky Lady*. The track of the REMUS AUV is also shown. Note that sampling passes were repeated throughout the duration of the ebb tide, with the REMUS sampling period coinciding with pass 4. The weather and sea state were calm, with a light offshore wind, and minimal swell.

[12] The density and velocity structure of the near-field region is characterized by a rapidly thinning and mixing fresh water layer located seaward of a bottom attached salt front (Figure 4). At the time of Pass 1, the salt front had not yet established itself at the estuary mouth, as ocean water was still present within the estuary. As the ebb progressed, the ocean water was expelled from the estuary, and sometime between Passes 1 and 2 a salt front was established near the bar located 400 to 600 m beyond the end of the jetties at the river mouth.

[13] The discharging river water was also characterized by a high coarse sediment load, which ultimately resulted in the conductivity cell of the OS200 malfunctioning owing to



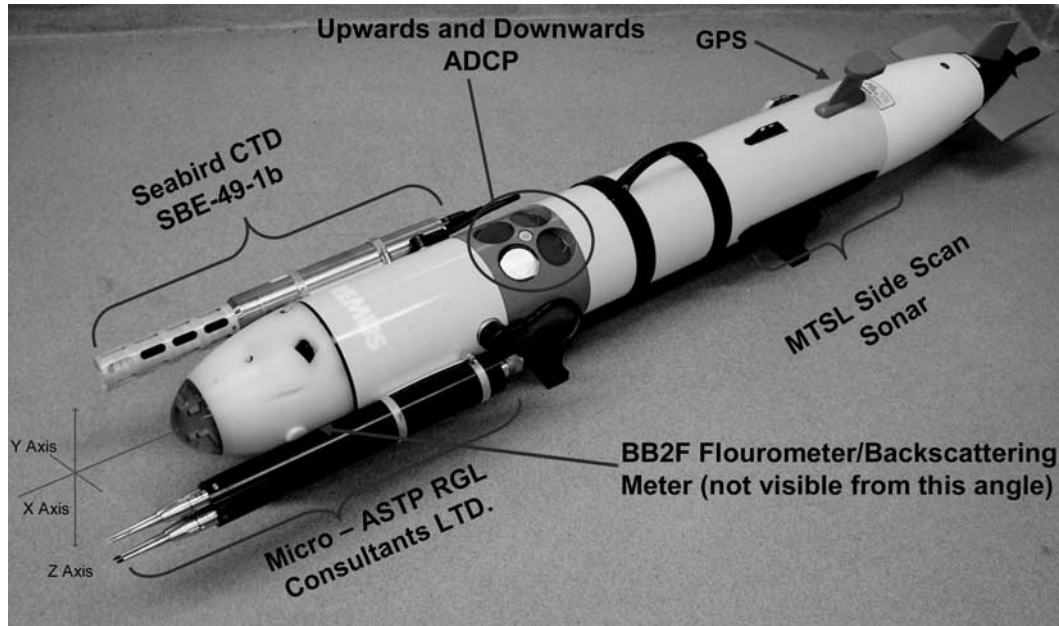


**Figure 3.** SMAST T-REMUS Autonomous Underwater Vehicle. It is 2 m long with a mass of 63 kg.

the lodging of fine sediment particles within the cell itself. During periods when the conductivity cell was compromised, salinity values were estimated on the basis of observed temperature salinity relationships, which exhibited good correlation, suggesting mixing occurring between two distinct and relatively homogeneous water masses, as shown in Figure 5. Such corrections were necessary for the majority of passes 2 and 4.

### 3. Techniques for Evaluating Terms in the TKE Equation

[14] Under the assumption of homogenous and stationary turbulence, the simplified turbulent kinetic energy equation can be written as [e.g., *Tennekes and Lumley, 1972*]

$$-\overline{u'_i u'_j} \frac{\partial \bar{u}_i}{\partial x_j} = \frac{g}{\rho_o} \overline{\rho' w'} + 2\nu \overline{e_{ij} e_{ij}}, \quad (1)$$

where  $u$  represents the components of the velocity vector,  $w$  represents vertical velocity (i.e.,  $u_3$ ),  $g$  is gravitational acceleration,  $\rho_o$  is a reference density of the fluid,  $\nu$  is kinematic viscosity,  $e$  represents the fluctuating rate of strain tensor, primes indicate fluctuating quantities, and the subscripts signify tensor notation. The term on the left-hand side of (1) is the shear production term,  $P$ . In the shear stratified environment of the near-field plume, velocity shear is present primarily in the vertical, so that the shear production term can be simplified as  $P = -\overline{u'w'} \frac{\partial \bar{u}}{\partial z}$ . The terms on the right hand side of (1) are the buoyancy flux,  $B$ , and the rate of TKE dissipation,  $\epsilon$ . The ratio of buoyancy flux to shear production is referred to as the flux Richardson number,  $Ri_f$ , which represents the fraction of TKE that is converted into potential energy through mixing against a density gradient. Laboratory studies [e.g., *Ivey and Imberger, 1991*] have suggested that the flux Richardson

number is constant and equal to approximately 0.18, for flows with a turbulent Froude number ( $Fr_T = (L_o/L_t)^{3/5}$ ) equal to 1. Recent observations in the near-field region of the Fraser River plume also support a value on the order of 0.2, which is consistent with the idea that turbulence along the shear stratified interface is driven mainly by the generation and decay of Kelvin-Helmholtz instabilities. Thus a direct measurement of any one of the terms in (1) should be sufficient to estimate all of the remaining terms.

#### 3.1. Control Volume Technique

[15] Velocity and density data from the four CTD/ADCP passes were interpolated onto uniform grids, with 40 m spacing in the horizontal, and 0.25 m in the vertical. Horizontal distance was measured from the river mouth, taken as the midpoint of the channel at the seaward end of the jetties. The control volume method described by *MacDonald and Geyer [2004]* was used to estimate turbulent quantities between each 40 m grid cell, which were then aggregated in groups to produce mean estimates across a 400 m distance. Quantities were estimated from salt and momentum budgets along a total of 31 density surfaces, with  $\sigma_t$  values ranging from 0 to 24.3 kg m<sup>-3</sup>, each surface corresponding to 1 psu differences in salinity. The density of the ambient ocean water was taken as 24.29 kg m<sup>-3</sup>, coincident with the highest valued density surface. Width expansion of the plume in the seaward direction was estimated by determining the width required at each section to conserve fresh water flux, as described by *MacDonald and Geyer [2004]*.

[16] Errors were attributed to each estimate using a Monte Carlo approach, whereby estimates were taken as the mean of 100 realizations for each grid point, each using a random set of assumptions. Errors due to time dependence were calculated on the basis of the predicted rate of change of surface elevation due to the tide, and randomly distributing the associated horizontal flux through the water column

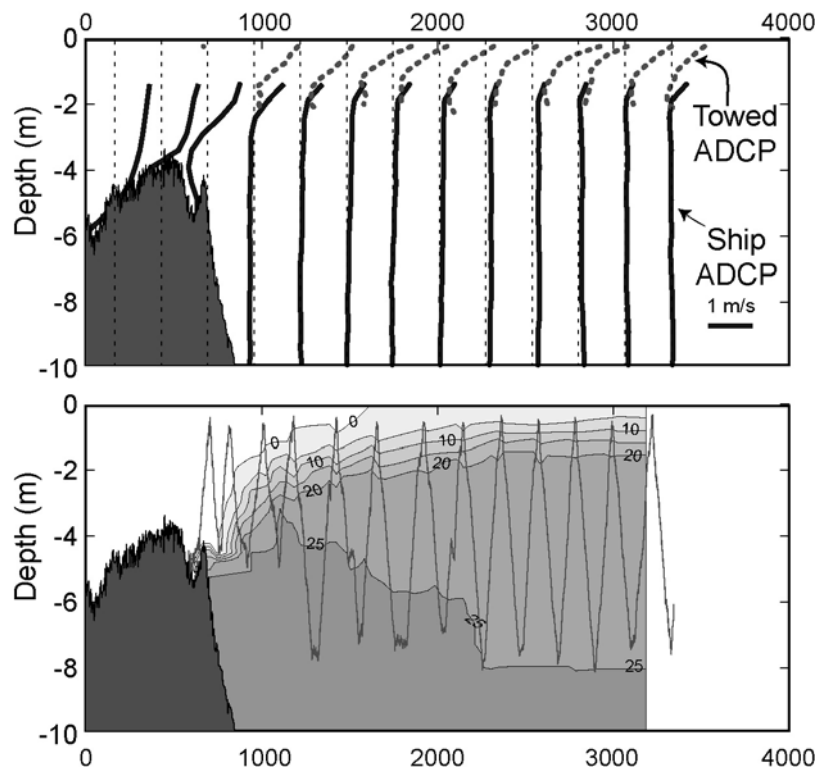


**Figure 4.** Profiles of velocity and density through the near-field plume, taken from Pass 4. (top) Individual velocity profiles from shipboard and towed ADCPs. (bottom) Density contours as determined from collected CTD data along tow-yo path shown. Seafloor is shown in both plots by the dark gray shading.

(i.e., in water of varying density class). Errors due to estimates of width expansion were accounted for by assuming a linear relationship between width and density, controlled by the expansion allowed at the base of the plume. This allowed for lighter fluid at the surface to spread faster than denser fluid at depth. The simplifying assumption of a linear width-density relationship is supported by *MacDonald and Geyer* [2004], who show that the resulting buoyancy flux estimates are relatively insensitive to the shape of the width expansion relationship, particularly for low- and mid-range density values. The degree to which the fluid at the bottom of the plume was allowed to expand was determined as a random value between zero and a value that resulted in a width expansion profile that was constant with density. Other errors accounted for included uncertainties in the value of the surface density, owing to tow-yo runs that may not have come directly to the surface, and potential vertical mismatch associated with lining up the density and velocity profiles.

[17] Estimates of  $\rho'w'$  were derived using the control volume technique to evaluate the density budget, by tracking fluxes of  $\sigma_t$  into and out of the control volume. It is also technically feasible to generate estimates of  $u'w'$  by tracking momentum fluxes in concert with a force balance on the surface of the control volume, as described by *MacDonald and Geyer* [2004]. This approach requires knowledge of the barotropic pressure gradient, which can be calculated assuming a layer of no motion at depth. Of the two estimates, the calculation of  $\rho'w'$  is considered to be more robust, owing to the complicated nature of the force balance

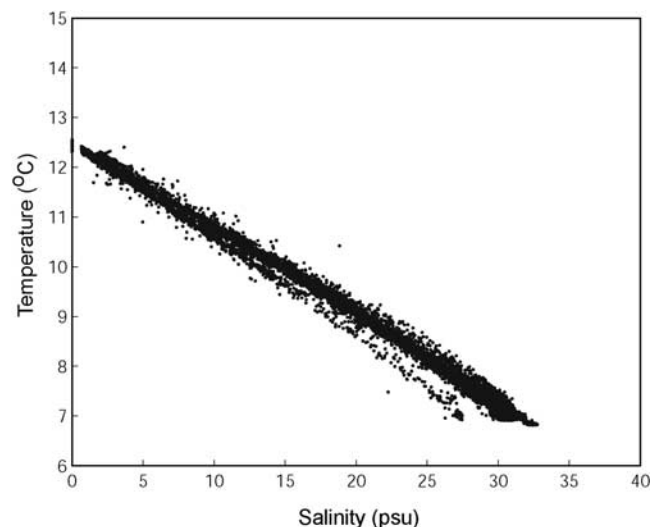


**Figure 5.** Temperature-salinity (TS) relationship for near-field plume region, based on measurements taken from 0716 to 0809 local time and 0956 to 1023 local time, both periods when the OS 200 CTD was functioning correctly. The linear relationship shown here was used to estimate salinity values based on temperature for periods when the conductivity cell was compromised owing to trapped sediment grains.

required to accurately constrain the  $\overline{u'w'}$  estimate. As such, only the  $\overline{\rho'w'}$  results are presented here, although both estimates show qualitatively similar trends.

[18] This technique allowed for the two dimensional structure of the Reynolds density flux term, leading directly to estimates of  $B$ , to be generated, providing a framework for understanding the evolution of the turbulent field across the first several kilometers of the near-field region. This is a significant advancement over the results presented by *MacDonald and Geyer* [2004], which provided vertical profiles at only one location within the near-field plume.

[19] Contours and representative vertical profiles of buoyancy flux, associated with passes 1 through 4, are shown in Figure 6. Note that these data are presented with respect to density, and not depth. Bold black lines in each contour plot represent density of the surface and bottom waters. Note the general trend of decreasing mixing away from the river mouth, with buoyancy flux decreasing by more than an order of magnitude in the first few kilometers seaward of the river mouth. Vertical profiles take a roughly parabolic shape peaking in intensity at midrange density values, and decaying toward zero at the surface and ocean density contours.

[20] The fact that turbulent quantities must decay to zero at the plume boundaries is a critical constraint of the calculation technique. By definition, a turbulent process is one that results in no net transport of fluid. For example, following the Reynolds averaging technique (i.e.,  $\overline{\rho w} = \overline{\rho'w'} + \overline{\rho} \overline{w}$ ), all net transport of fluid on the right hand side is accomplished by the advective term,  $\overline{\rho} \overline{w}$ , while the  $\overline{\rho'w'}$  term represents the transport of density accomplished only through a compensating exchange of higher and lower density fluids. Therefore focusing on the ocean density contour, which serves as the bounding surface separating plume waters from an ocean assumed to be of uniform density, any turbulent transport of ambient ocean water upward through that surface would have to be compensated by an equal amount of plume water mixed downward, ultimately resulting in a displacement of the ocean density contour in the downward direction. Thus there can be no turbulent transport across the bottom boundary of the plume. There is, however, a significant upward directed advective transport [see *MacDonald and Geyer*, 2004] of ambient ocean water across the bottom boundary of the plume, resulting in an upwelling which is necessary to satisfy mass conservation and to feed all of the turbulent mixing processes occurring higher in the water column.

### 3.2. Turbulence AUV

[21] Direct values of the TKE dissipation rate were obtained by using the SMAST AUV, T-REMUS vehicle. T-REMUS is a custom designed, extended REMUS, 1.9 m in length with a mass of 63 kg. Mounted forward on the vehicle (see Figure 3) is the Micro ASTP developed by RGL Consultants (now Rockland Scientific International) of Victoria, BC. The Micro ASTP turbulence package consists of two orthogonal thrust probes, two FP07 fast response thermistors, three orthogonal accelerometers and a fast response pressure sensor. Also contained on the T-REMUS vehicle are an upward and downward looking 1.2 MHz ADCP, a FASTCAT CTD, a Wet Labs

BB2F Combination Spectral Backscattering Meter/Chlorophyll Fluorometer, and a variety of “hotel” sensors measuring pitch, roll, yaw, and many other internal dynamical characteristics of the T-REMUS vehicle. This suite of sensors allows quantification of the key dynamical and kinematical turbulent and fine-scale physical processes. The turbulent and fine-scale parameters which can be estimated from the data collected by the T-REMUS include: the turbulent dissipation rate, fine-scale velocity shear and fine-scale stratification [see *Levine and Lueck*, 1999; *Goodman et al.*, 2006].

[22] Turbulent dissipation rate  $\varepsilon$  is estimated by calculating

$$\varepsilon = \frac{15}{4} \left\langle \frac{\partial v}{\partial x} + \frac{\partial w}{\partial x} \right\rangle, \quad (2)$$

where  $x$  is the along track direction, and  $v$  and  $w$  are the cross-track and vertical velocity components, respectively. Correction for vehicle motion and sensor vibration is performed by coherently subtracting the three components of acceleration using a Weiner function filter (R. Lueck, personal communication, 2006) on the two components of shear in equation (2). An analogous procedure for spectral correction is given by *Goodman et al.* [2006]. Equation (2) involves the assumption of isotropy at the smallest (Kolmogorov) scales of motion. *Yamazaki and Osborn* [1993] have shown that this assumption is valid for a value of  $\frac{\varepsilon}{\nu N^2} > 100$ .

[23] Dissipation rate was calculated by averaging the two shear terms of (2) over 5 meters horizontally, which typically corresponded to 10 centimeters vertically. The range of wave numbers making the dominant (90%) contribution to the dissipation rate is expected to be near the peak in the shear spectra which is of order 0.1 times the Kolmogorov wave number [*Lueck et al.*, 2002]. For our data this peak occurs between 10 to 20 cyc/m (or 5 cm to 10 cm length scale). Using an average over 5 meters in the horizontal yields an effective number of degrees of freedom of order 20. (The peak in the shear spectra tended to occur at wave numbers  $> 20$  cyc/m for  $\varepsilon > 10^{-7} \text{ m}^2 \text{ s}^{-3}$ .) Shear spectra corresponding to  $\varepsilon > 10^{-7} \text{ m}^2 \text{ s}^{-3}$  had reasonable universal *Nasmyth* [1970] spectra with the  $v$  and  $w$  shear tending to be the same magnitude. Thus for this data set we estimate that noise levels were sufficiently low to trust dissipation rate values  $\varepsilon > 10^{-7} \text{ m}^2 \text{ s}^{-3}$  within calculated error bounds. We calculated 90% error bounds by subsampling the data over a 0.4 m horizontal range (shear probe data being sampled at 500 Hz and the shear variance averaged over 200 points) and forming a histogram (pdf) of the subsampled  $\varepsilon$  values using (2). The resulting raw values of  $\varepsilon$  tended to follow a log normal distribution [*Gregg*, 1987], as expected. For dissipation rate values  $\varepsilon > 10^{-7} \text{ m}^2 \text{ s}^{-3}$ , approximately 70% had values of  $\frac{\varepsilon}{\nu N^2} > 20$ , a boundary where active turbulence is expected to occur [*Itswiere et al.*, 1993]. For this range of  $\frac{\varepsilon}{\nu N^2}$  values the assumption of isotropy should lead to errors no greater than 40% [*Yamazaki and Osborn*, 1990, 1993], which is typically of the same order or less than the error estimates described above.



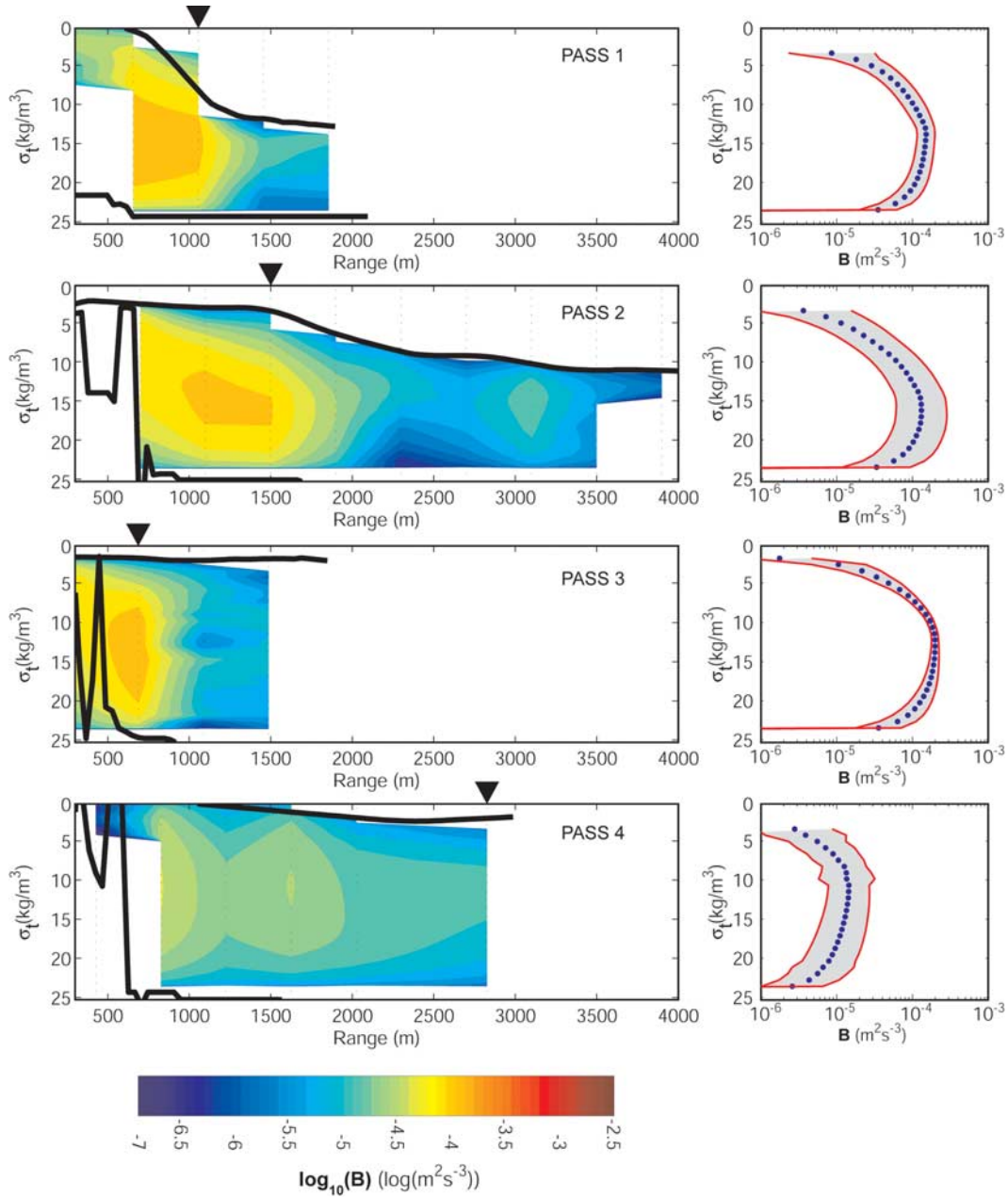


**Figure 6.** Contours and representative vertical profiles of buoyancy flux, as estimated from the control volume method along the four passes shown in Figure 2. Contour plots are shown on a log scale as indicated, and are plotted against density on the vertical scale. Thick black lines in the contour plots represent surface and bottom densities. Centerpoint locations of the 400-m-long control volumes for which estimates were generated are shown by the dotted lines in the contour plots. One representative profile, taken at the location indicated by the black triangles above each contour plot, is plotted for each pass. Error bars represent one lognormal standard deviation of the variability, as described in the text.

[24] The vehicle was programmed to sample in a 1 degree yo-yo pattern along the track shown in Figure 2, oscillating between depths of approximately 1 m and 3.8 m, and completing one down and up cycle in approximately 250 m in the horizontal. A contour of TKE dissipation rates, plotted versus range and density, is presented in Figure 7. Note that the track of the AUV did not penetrate into the plume above the  $\sigma_t = 19 \text{ kg m}^{-3}$  contour. However, significant structure in dissipation rate can be observed near

the base of the plume within this data set. Similarly to the control volume derived data, a decrease of approximately 1 to 2 orders of magnitude in dissipation rate is observed across the first several km seaward of the mouth.

### 3.3. Numerical Modeling

[25] A numerical model of the Merrimack River plume was developed using the Regional Ocean Modeling System (ROMS). A curvilinear grid was constructed with grid

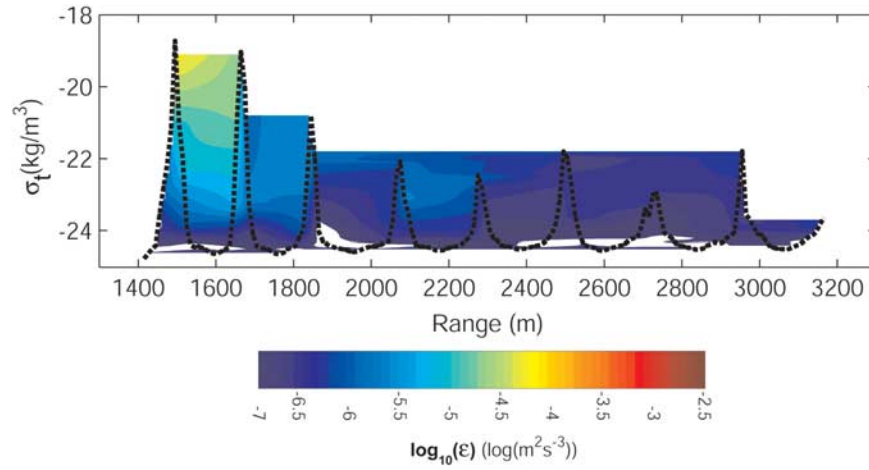


**Figure 7.** Contours of dissipation rate calculated from the turbulence AUV. Dashed line represents path of AUV through the density structure of the plume.

spacing on the order of 20 m near the river mouth, resulting in 15 grid points spaced evenly between the jetties at the mouth of the estuary. An  $s$ -coordinate system ( $\theta_s = 5.0$ ,  $\theta_b = 0.1$ ,  $h_c = 1.0$ ) with 30 grid points, was used in the vertical, with enhanced resolution near the surface. This resulted in 14 to 24 grid points above 2 m depth, and 10 to 17 grid points above 1 m depth, depending on location (highest resolution was obtained over the sill approximately 500 m

seaward of the mouth). Turbulence closure was accomplished using the generic length scale (GLS) model [Umlauf and Burchard, 2003]. Preliminary results show that the model is insensitive to the closure scheme (the  $k-\epsilon$  closure is shown here), but is slightly sensitive to the form of the stability functional (shown here, Canuto-A).

[26] ROMS is a hydrostatic model. However, since turbulence from shear mixing is not explicitly resolved, the

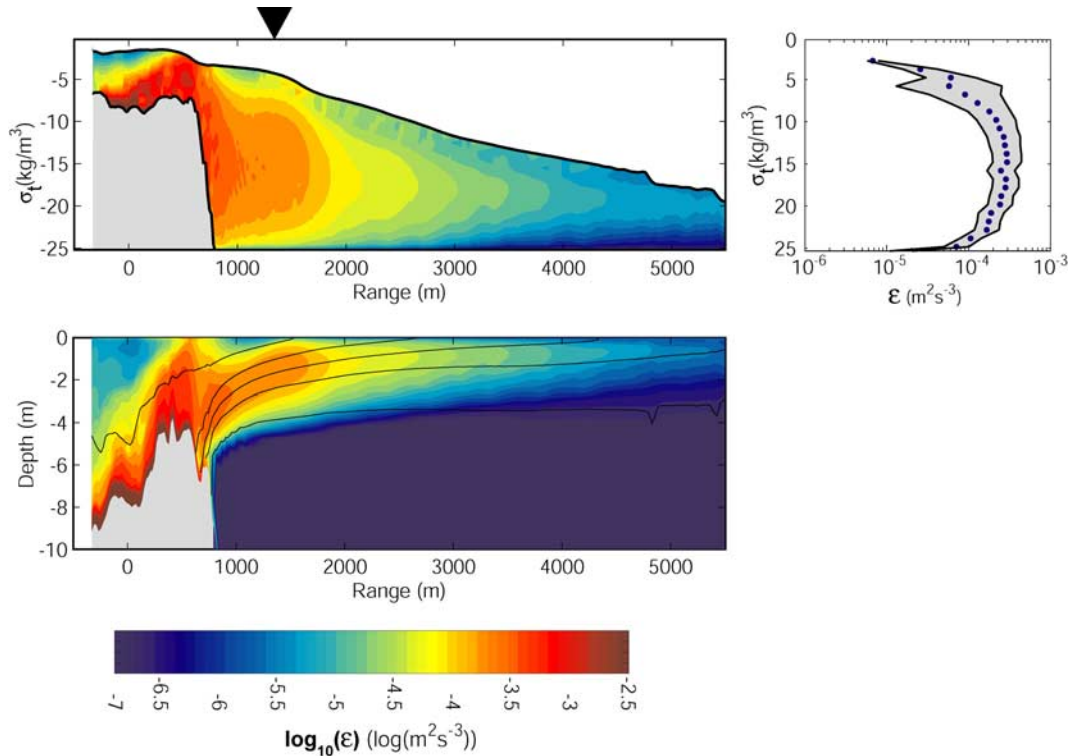


**Figure 8.** Contours of dissipation rate from numerical model, in both density space and vertical space. A representative profile of the dissipation rate (location indicated by black triangle) is shown to the right, similarly to Figure 6. Error range represents one lognormal standard deviation of five profiles extracted from the model during the latter half of the ebb tide. Each profile was separated by a half hour.



hydrostatic assumption should remain valid. Furthermore, given the small aspect ratio (vertical to horizontal length scales) of the flow, the complex dynamics near the front should be adequately modeled using hydrostatic techniques [e.g., O'Donnell *et al.*, 1998].

[27] The model was run with a 1.3 m amplitude M2 tide, and initiated with ocean water within the estuary, and a mid ebb tidal phase. A constant freshwater inflow of  $1294 \text{ m}^3 \text{ s}^{-1}$  was used, consistent with the gauged flow at Lowell, MA during the field study. Model results presented were averaged over the second half of the first full ebb tide. Figure 8 (top) shows contours of the temporally averaged TKE dissipation rate along with a representative profile. Figure 8 (bottom) shows similar data plotted against depth. These plots are taken along a line due east from the river mouth. Spatial patterns and patterns in density space similar in structure and magnitude to those observed for the control volume and microstructure measurements are apparent.

## 4. Discussion

### 4.1. Method Comparison

[28] The contour plots shown in Figures 6, 7 and 8 show qualitatively similar results for the two observational techniques and the numerical simulation. A more quantitative assessment can be generated by comparing specific values. For these purposes, the buoyancy flux estimates derived from the control volume technique have been converted to dissipation rates assuming a constant  $Ri_f$  value equal to 0.18, and compared to the direct estimates from the turbulence AUV, and the numerically generated dissipation rates produced by the ROMS model. Figure 9 shows comparison of these three estimates following several distinct isopycnals representing the lower portion of the plume. The isopycnals shown in Figure 9 span the region where viable estimates from all three methods were produced. The control volume estimates shown are from Passes 2 and 4, which are the longest of the four passes. Pass 4 also coincided with the REMUS sampling period.

[29] These comparisons show similar trends between the estimates, with reasonably good agreement between the three methods within specific portions of the domain. The model data represent an average of five snapshots covering a 2 hour period during mid to late ebb, roughly coinciding with the timing of the two control volume estimates shown. Considering the temporal variability evident in the control volume estimates, the model and control volume method appear to be in good agreement. With the exception of the 1000 to 1500 m region, which is a region of rapid isopycnal adjustment within the liftoff region of the plume, the numerical results are generally within one standard deviation of both of the control volume passes. Even within the liftoff region, agreement within one standard deviation would be achieved if the mean of the control volume passes were considered. Both methods show a decreasing trend in dissipation rate with distance from the mouth.

[30] Comparisons with results from the turbulence AUV appear strongest at lower densities, with error bars overlapping at  $\sigma_t = 19$  and  $\sigma_t = 20 \text{ kg m}^{-3}$ . At the higher densities, the AUV estimates appear lower than the control volume and model estimates by 1 to 2 orders of magnitude, with the exception of two locations (at approximately 1600

and 2300 m) where closer agreement is observed. The reasonable comparison between the model results and the control volume estimates stands in contrast to their widening gap with the AUV estimates at higher densities.

[31] There are several potential causes for the discrepancies observed at higher densities, and it is important to understand the differences in the various measurement and modeling techniques. The AUV is capable of measuring instantaneous, local dissipation rates, whereas the control volume and model estimates both present a larger-scale mean dissipation rate. The observed instantaneous values may be lower than the true “ensemble” mean values due to the combined effects of the expected log normality of  $\epsilon$  statistics as well as the effects of local heterogeneity and non stationarity [e.g., Gregg, 1987; Gibson, 1991]. The existing data set is too limited in time and space to provide conclusive evidence in this regard, although the AUV observed values at  $\sigma_t = 19 \text{ kg m}^{-3}$  are somewhat higher than the other estimates and could be suggestive of an isolated burst. An inhomogeneous turbulence field appears reasonable, considering that bursts of intensity 1 order of magnitude larger than the mean value of dissipation would be required over an area equaling only 10% of the total. Given that mixing processes in the near-field region are likely driven by the generation of Kelvin-Helmholtz instabilities [e.g., Geyer and Farmer, 1989; MacDonald and Geyer, 2004], which evolve in a coherent fashion before a sudden and intense decay into turbulence, the idea of an inhomogeneous turbulence field seems even more plausible.

[32] There also exists a fundamental difference between the two measurement techniques related to the quantities measured. While the AUV provides direct estimates of TKE dissipation rates, the control volume method, as presented here, provides an inferred estimate of the buoyancy flux term in equation (1), which is then related to dissipation, assuming steady state and homogeneous conditions, using a constant value of  $Ri_f$ . Therefore an alternative explanation for the discrepancy between the two measurement techniques could be a breakdown of the homogeneous and steady state assumptions near the base of the plume, resulting in additional terms in equation (1) to account for the transport of TKE [e.g., Tennekes and Lumley, 1972], and ultimately invalidating the constant  $Ri_f$  approach.

[33] Finally, it should also be noted that the control volume method is expected to be less accurate at the base of the plume, owing to the technique's sensitivity to two factors: (1) the density value chosen to represent ambient ocean water, and (2) the assumptions used to characterize width expansion, both of which have a more significant affect near the base of the plume.

[34] The trends observed along specific isopycnals are reinforced in Figure 10, which presents a comparison between the peak dissipation rates generated from both the control volume technique and the numerical model. Here the results from all four control volume passes are represented. Again, we see good agreement across most of the regime, although larger variability is seen among the individual control volume estimates between 1 to 2 km. Although the four passes are distributed across the ebbing tide, the control volume results from the various passes do not suggest a simple temporal evolution. Rather, it is likely that the observed differences are indicative of the fact that

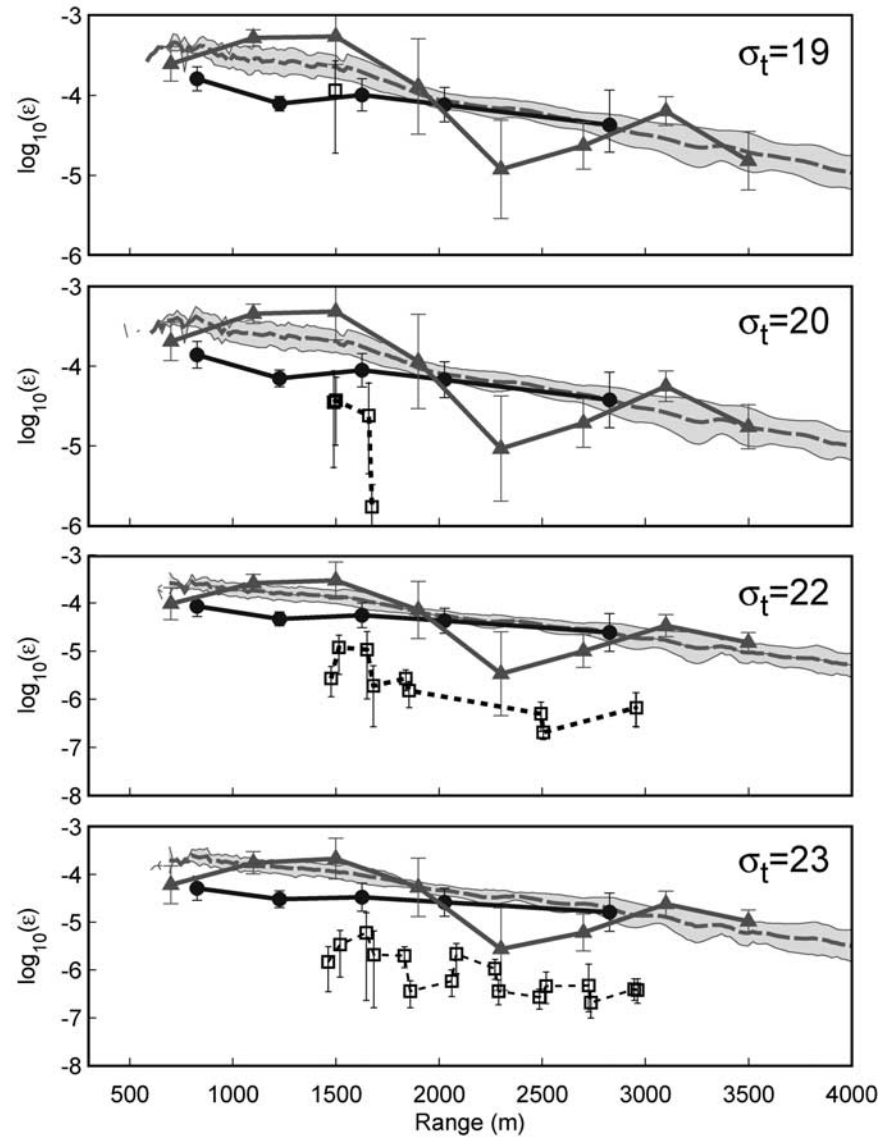


**Figure 9.** Comparisons of epsilon estimates along selected isopycnals, as shown. Control volume estimates are taken from Passes 2 and 4, and represented by solid triangles and circles, respectively, with error bars (one lognormal standard deviation). Turbulence AUV estimates are represented by the open squares with 90% error bars, and the model data are shown by the dashed line and shaded error region (one lognormal standard deviation). Note that the vertical scale in the bottom two plots covers a broader range of dissipation rates than in the top two plots.

the region between 1 and 2 km represents a transition zone characterized by a steeply inclined pycnocline. In this region, the plume is accelerating and thinning, suggestive of rapid lateral spreading, which appears to result in a natural variability in TKE dissipation. Seaward of this ‘lift-off’ zone, the plume thickness stabilizes and then slowly begins to deepen, suggesting a decrease in the rate of lateral spreading. Overall, the model appears to perform well in the near-field region, accurately predicting the two decade decrease in  $\epsilon$  observed across the first 4 km and seen also in Figures 6 and 7, although the natural variability

observed within the lift-off zone yields a less robust comparison than in the more seaward regions of the near-field plume.

#### 4.2. Near-Field Dynamics

[35] The data presented above reveal the structure of turbulence in a near-field plume region in significantly more detail than has been observed previously. In an attempt to understand the turbulence generating mechanism with respect to the energetics of the mean flow, *MacDonald and Geyer* [2004] suggested the following scaling, related

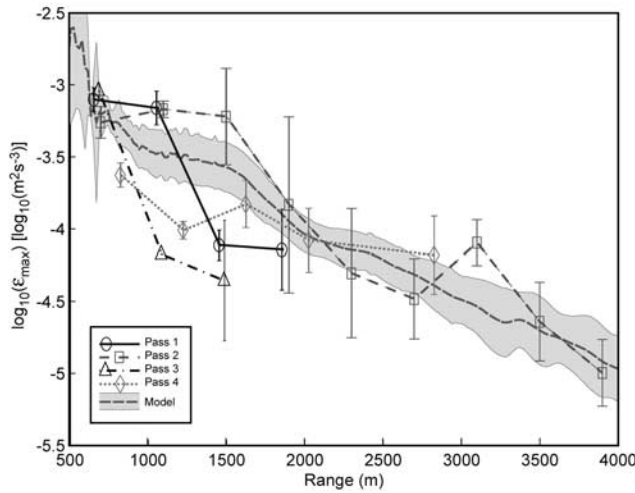


**Figure 10.** Comparison of maximum dissipation rate (with respect to a vertical profile), between the four control volume passes and the model. Error bars and shaded error region represent one lognormal standard deviation.

to an interfacial drag coefficient, for the near-field region [after Ivey and Imberger, 1991]:

$$\frac{\varepsilon}{g'\Delta u} = \frac{(1 - Ri_f)}{Ri_g} C_{Di} \sim 2 \times 10^{-3}, \quad (3)$$

where  $Ri_g = -\frac{g}{\rho} \frac{\partial \rho}{\partial z} \left( \frac{\partial u}{\partial z} \right)^{-2}$  is the gradient Richardson number,  $Ri_f$  the flux Richardson number, and  $C_{Di}$  is an interfacial drag coefficient. In the context of a drag coefficient, the expression in (3) represents the fraction of mean flow energy that is effectively converted to TKE. The scaling originally presented by MacDonald and Geyer [2004] and Ivey and Imberger [1991] is based primarily on dimensional analysis, and it is instructive to look more closely at a physical interpretation of (3).

[36] The drag coefficient expression in the middle of (3) can be easily derived (for a two-dimensional flow) by rearranging the quadratic drag formulation for interfacial shear,  $\tau_i = \rho C_{Di} (\Delta u)^2 = \rho u' w'$ , and incorporating the definition of TKE production from (1), as well as  $Ri_f$  and  $Ri_g$ . This approach is equivalent to considering the rate at which energy is extracted from the mean flow within a given volume of fluid,

$$\Gamma = \rho A C_{Di} (\Delta u)^3 = \rho P V, \quad (4)$$

where  $\Gamma$  represents power,  $A$  is area,  $V$  is volume and  $P$  is the turbulent shear production. From this approach, it is clear that the value of  $\varepsilon$  in (3) should be taken as the mean value of TKE dissipation over the volume, although the constant in (3) was originally estimated on the basis of maximum dissipation values. It should also be noted that (4) reduces directly to an alternative expression,  $P = C_{Di} (\Delta u)^3 h^{-1}$ , where  $h$  is the vertical dimension of the volume in question. This expression can be combined with an estimate of dissipation scaled directly from the turbulent velocity ( $u_t$ )

and length scales [e.g., Tennekes and Lumley, 1972]. If the turbulent length scale is assumed equal to the Ozmidov scale, this yields

$$C_{Di} \frac{(\Delta u)^3}{h} (1 - Ri_f) = \frac{u_t^3}{L_o}, \quad (5)$$

which, under the assumption of constant velocity shear, can be reduced to a form similar to (3). Thus it is clear that the expression in (3) adequately represents the important physics in a two-dimensional framework.

[37] The original estimation of the constant value on the right hand side of (3) was determined on the basis of a small number of point measurements within the near-field region of the Fraser River plume, and, as mentioned above, was based on maximum observed dissipation rates. Despite the limited basis of this estimate, it is fairly consistent with data presented by Dallimore et al. [2001] for turbulence associated with a saline underflow into a freshwater lake, and by Orton and Jay [2005] for turbulence observed near the surface front of the Columbia River plume. However, when compared to the dissipation rates observed within this study (Figure 11), the effectiveness of (3) appears to diminish with increased distance from the mouth. Note that the data plotted in Figure 11 are based on mean dissipation rates

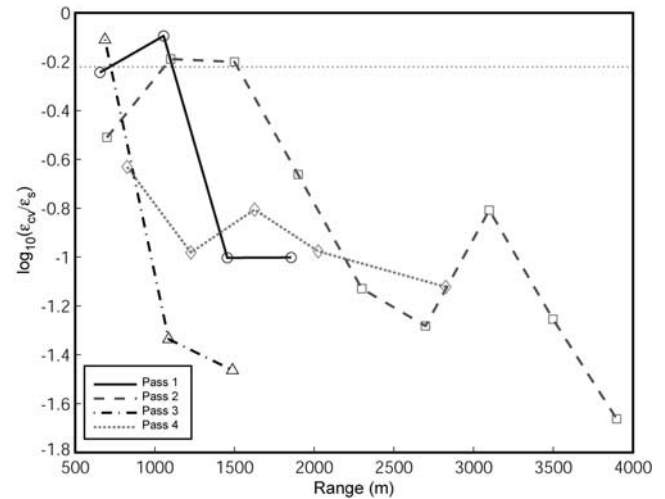


**Figure 11.** Ratio of mean observed dissipation rate, as calculated from the control volume method, to a dissipation rate scaled as  $\varepsilon \sim (2 \times 10^{-3}) g' \Delta u$  [e.g., MacDonald and Geyer, 2004]. Logarithm of ratio is plotted, so that one to one correspondence between the observed and scaled dissipation rates is characterized by a value of 0. Note that the constant ( $2 \times 10^{-3}$ ) was estimated by MacDonald and Geyer [2004] on the basis of maximum observed dissipation rate. However, a physical interpretation of the scaling suggests that the mean dissipation rate is more appropriate, as described in the text. The present data set suggests that the mean dissipation rate scales as approximately 0.6 times the maximum dissipation, so  $\log_{10}(0.6)$  has been plotted for reference (dotted line). Observations from three of the four passes match the scaling well near the front, but all decrease substantially farther out in the plume.



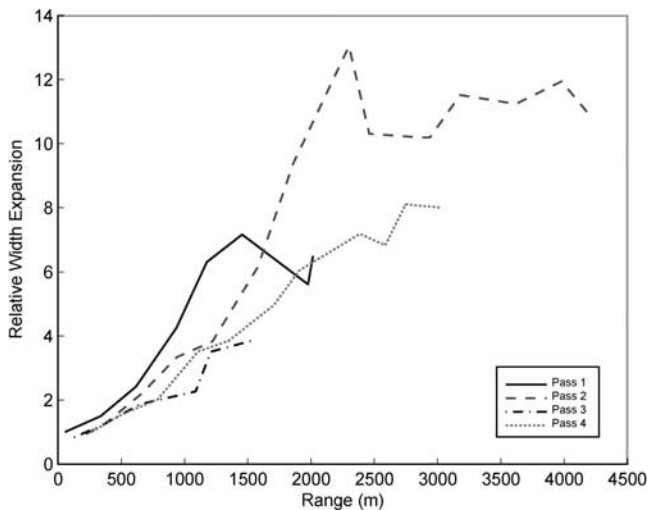


**Figure 12.** Minimum envelope of relative width expansion derived from control volume estimates for Passes 1 through 4. Note that the gradient of expansion seems to decrease between 1500 and 3000 m from the mouth.

observed across the entire plume depth, and that the dotted line represents an approximate scaling factor between the mean and maximum dissipation values. The data plotted in Figure 11 suggest that the ratio ( $\epsilon/g'\Delta u$ ) may not be constant, as suggested in (3).

[38] The near-field plume is a complicated region, with the flow field undergoing rapid adjustments, not only in the vertical, as shown in Figure 4, but also in the horizontal [see *Hetland, 2005*]. In the lift-off region, rapid shoaling of the plume can cause significant acceleration. However, horizontal divergence of streamlines within the plume, driven by lateral pressure gradients resulting from the density difference between the plume waters and ambient ocean waters, can temper the shoaling-driven acceleration. The presence of active turbulence not only produces a drag force on the plume waters, directly decelerating the advancing plume, but may also play a role in modifying the rate of width expansion due to a direct influence on the lateral pressure gradient.

[39] It is clear that both vertical and lateral effects are important to the evolution of the plume and the turbulent field. The gradient Richardson number characterizes many of the vertical influences, and its importance to the value of the dissipation rate is apparent from the expression in (3), and the physical discussion presented above. However, physics associated with the lateral dynamics are not explicitly included in (3), which was derived within a two-dimensional framework. A Buckingham-Pi scaling analysis of the three-dimensional near-field plume problem suggests that there should be three independent nondimensional parameters, which can be accounted for by the ratio  $\frac{\epsilon}{g'\Delta u}$ , the gradient Richardson number,  $Ri_g$ , and a third parameter representing the rate of width expansion (i.e.,  $\frac{\partial b}{\partial x}$ ). Given that the value of  $Ri_g$  is relatively constant across the near-field region, it is likely that the rate of width expansion may

play the primary role in adjusting the value of the constant in (3), particularly given that the inferred width expansion associated with the control volume calculations suggests that the rate of width expansion may decrease significantly seaward of approximately 1500 to 2500 m (Figure 12). This trend is particularly apparent in passes 1 and 2.

## 5. Conclusions

[40] Estimates of TKE dissipation rates derived from a control volume approach, AUV microstructure data, and a highly resolved numerical model show reasonably good agreement over the majority of the shear stratified near-field plume region. Some significant discrepancies between the control volume and microstructure data near the base of the plume may suggest that small-scale heterogeneity is present in the turbulent field, with localized bursts of turbulence responsible for the majority of mixing. Alternatively, the discrepancies may also point toward a breakdown in the steady state and homogenous assumptions inherent in equation (1), invalidating the comparison of directly estimated dissipation rates with rates inferred from buoyancy flux values using a constant  $Ri_g$ . The performance of the model, using standard turbulence closure techniques, is encouraging.

[41] The data presented underscore the complexity of the near-field region, particularly with regards to the interaction between plume spreading and mixing, and the evolution of the plume through the rapidly accelerating lift-off region. Future observational and numerical work associated with the Merrimack River plume will focus on these issues, and their relationship to the structure of the turbulent field, in order to more fully understand the behavior of the plume, and the mechanisms responsible for mixing in the region.

[42] **Acknowledgments.** The authors thank F. Chen, J. Yarnac, Z. Wang, and R. Rock for their help during the field efforts. This work was funded by National Science Foundation grant OCE-0550096. This manuscript is contribution 07-0402 in the SMAST Contribution Series, School for Marine Science and Technology, University of Massachusetts, Dartmouth.

## References

- Burchard, H., and H. Baumert (1995), On the performance of a mixed-layer model based on the  $k-\epsilon$  turbulence closure, *J. Geophys. Res.*, **100**(C5), 8523–8540.
- Burchard, H., K. Bolding, T. P. Rippeth, A. Stips, J. H. Simpson, and J. Sündermann (2002), Microstructure of turbulence in the northern north sea: comparative study of observations and model simulations, *J. Sea Res.*, **47**, 223–238.
- Chen, F., and D. G. MacDonald (2006), Role of mixing in the structure and evolution of a buoyant discharge plume, *J. Geophys. Res.*, **111**, C11002, doi:10.1029/2006JC003563.
- Dallimore, C. J., J. Imberger, and T. Ishikawa (2001), Entrainment and turbulence in saline underflow in Lake Ogawara, *J. Hydraul. Eng.*, **127**(11), 937–948.
- Galperin, B., L. H. Kantha, L. H. Hassid, and A. Rosati (1988), A quasi-equilibrium turbulent energy model for geophysical flows, *J. Atmos. Sci.*, **45**, 5562.
- Geyer, W. R., and D. M. Farmer (1989), Tide-induced variation of the dynamics of a salt wedge estuary, *J. Phys. Oceanogr.*, **19**, 1060–1072.
- Gibson, C. H. (1991), Turbulence, mixing, and heat flux in the ocean main thermocline, *J. Geophys. Res.*, **96**(C11), 20,403–20,420.
- Goodman, L., E. Levine, and R. Lueck (2006), On measuring the terms of the turbulent kinetic energy budget from an AUV, *J. Atmos. Oceanic Technol.*, **23**, 977–990.
- Gregg, M. C. (1987), Diapycnal mixing in the thermocline: A review, *J. Geophys. Res.*, **92**(C5), 5249–5286.

- Hetland, R. D. (2005), Relating river plume structure to vertical mixing, *J. Phys. Oceanogr.*, **35**, 1667–1688.
- Itswiere, E. C., J. R. Koseff, D. A. Bruggs, and J. H. Ferziger (1993), Turbulence in stratified shear flows: Implication for interpreting shear-induced mixing in the ocean, *J. Phys. Oceanogr.*, **23**, 1508–1522.
- Ivey, G. N., and J. Imberger (1991), On the nature of turbulence in a stratified fluid. Part I: The energetics of mixing, *J. Phys. Oceanogr.*, **21**, 650–658.
- Kay, D. J., and D. A. Jay (2003), Interfacial mixing in a highly stratified estuary: 1. A “method of constrained differences” approach for the determination of the momentum and mass balances and the energy of mixing, *J. Geophys. Res.*, **108**(C3), 3073, doi:10.1029/2000JC000253.
- Levine, E. R., and R. G. Lueck (1999), Turbulence measurements from an autonomous underwater vehicle, *J. Atmos. Oceanic Technol.*, **16**, 1533–1544.
- Levine, E. R., D. Connors, R. Shell, and R. Hanson (1997), Autonomous underwater vehicle-based hydrographic sampling, *J. Atmos. Oceanic Technol.*, **14**, 1444–1454.
- Lueck, R. G., F. Wolk, and H. Yamazaki (2002), Oceanic velocity turbulence measurements in the 20th century, *J. Oceanogr.*, **58**, 153–174.
- MacDonald, D. G., and W. R. Geyer (2004), Turbulent energy production and entrainment at a highly stratified estuarine front, *J. Geophys. Res.*, **109**, C05004, doi:10.1029/2003JC002094.
- Nasmyth, P. W. (1970), Ocean turbulence, Ph.D. thesis, Univ. of B. C., Vancouver, B. C., Canada.
- O'Donnell, J., G. O. Marmorino, and C. L. Trump (1998), Convergence and downwelling at a river plume front, *J. Phys. Oceanogr.*, **28**, 1481–1495.
- Orton, P. M., and D. A. Jay (2005), Observations at the tidal plume front of a high-volume river outflow, *Geophys. Res. Lett.*, **32**, L11605, doi:10.1029/2005GL022372.
- Osborn, T. R. (1974), Vertical profiling of velocity microstructure, *J. Phys. Oceanogr.*, **4**, 109–115.
- Richardson, L. F. (1920), The supply of energy from and to atmospheric eddies, *Proc. R. Soc., Ser. A*, **97**, 354–373.
- Rodi, W. (1987), Examples of calculation methods for flow and mixing in stratified fluids, *J. Geophys. Res.*, **92**(C5), 5305–5328.
- Siddon, T. F. (1965), A turbulence probe utilizing aerodynamic lift, *Rev. Sci. Instrum.*, **42**, 653–656.
- Tennekes, H., and J. L. Lumley (1972), *A First Course in Turbulence*, MIT Press, Cambridge, Mass.
- Umlauf, L., and H. Burchard (2003), A generic length-scale equation for geophysical turbulence models, *J. Mar. Res.*, **61**, 235–265.
- Wright, L. D., and J. M. Coleman (1971), Effluent expansion and interfacial mixing in the presence of a salt wedge, Mississippi River Delta, *J. Geophys. Res.*, **76**(36), 8649–8661.
- Yamazaki, H., and T. Osborn (1990), Dissipation estimates for stratified turbulence, *J. Geophys. Res.*, **95**(C6), 9739–9744.
- Yamazaki, H., and T. Osborn (1993), Erratum: “Dissipation Estimates For Stratified Turbulence” [*Journal of Geophysical Research*, **95**, 9739–9744 (1990)], *J. Geophys. Res.*, **98**(C7), 12,605–12,606.

---

L. Goodman and D. G. MacDonald, Department of Estuarine and Ocean Sciences, School for Marine Science and Technology, University of Massachusetts Dartmouth, 706 South Rodney French Boulevard, New Bedford, MA 02744-1221, USA. (dmacdonald@umassd.edu)

R. D. Hetland, Department of Oceanography, Texas A&M University, College Station, TX 77843, USA.